Eur. Phys. J. D **40**, 377–385 (2006)
DOI: 10.1140/epjd/e2006-00184-1

THE EUROPEAN PHYSICAL JOURNAL D

Adaptive clustering of a quantum solvent: the LiH^+ cation in bosonic helium from stochastic calculations

C. Di Paola, E. Bodo, and F.A. Gianturco[a]

Department of Chemistry, University of Rome La Sapienza, Piazzale A. Moro 5, 00185 Rome, Italy

Received 23 May 2006 / Received in final form 4 July 2006
Published online 5 August 2006 –

Abstract. Calculations of the quantum structures describing the initial solvation shells of bosonic helium atoms around a polar, ionic system like LiH^+ are reported, together with the corresponding quantum energies. The calculations were carried out using the Diffusion Monte Carlo (DMC) approach and parametric trial functions. Its final radial and angular distributions for clusters of varying size are analysed and discussed. The solvation of this ionic dopant is shown to occur in a way which is strongly affected by the orientational induction forces between the latter molecule and the solvent atoms, indicating the onset of "snowball" structures at the location of the dopant and the clear distinction between "heliophilic" and "heliophobic" regions of microsolvation.

PACS. 36.40.-c Atomic and molecular clusters

1 Introduction

Since its discovery in 1954 [1] matrix isolation in crystals has become a powerful experimental technique which is particularly useful in studies of transient species, such as molecular radicals, and ions [2]. Seeded supersonic beams provide another technique which has been used to cool free molecules and to produce free molecular complexes and clusters. Recently, a combination of the two techniques led to the development of a new experimental approach, the isolation of species in ultracold ($T = 0.37$–0.15 K) helium droplets, which are made of up to 10^3 to 10^8 helium atoms [3–6]. The fluid helium droplets can readily pick up atoms and molecules and can form complexes from the species embedded in their interiors, or on their surfaces, thereby providing unique experimental opportunities: extensive experiments conducted in the last 10 years have, in fact, demonstrated helium droplets to be the ultimate matrix for the 'ultracold' experiments. They are characterized by extremely low temperatures, little matrix broadening, and offer unique possibilities to synthesize new molecular complexes [7]. It is therefore the fundamental difference in the behavior of classical liquids or solids and the quantum liquid helium, respectively, that determines the extraordinary differences in their properties as spectroscopic matrices.

In the case of liquid ^{4}He, impurities quickly coagulate to form clusters that either rise to the surface or fall to the bottom of the reaction vessel. Contemporary methods of immersing foreign atoms into bulk liquid helium usually involve laser induced ablation of metals into the liquid [8]. This method makes it possible to obtain rather large transient concentrations of 'metal atoms' in the liquid, although, to date the successful implantation of species other than metals, in particular of intact molecules, into bulk liquid helium has not been possible. One recent experimental development involves first embedding the foreign species inside large helium droplets formed in a pulsed beam and then directing the beam at the surface of the helium bath [9]. The fact that also ions can be captured inside helium nanodroplets opens the way to a new class of experiments which will provide a unique opportunity for testing the accuracy of the microscopic theories [10].

As mentioned above, laser ablation of in situ metals has recently made it possible to immerse a large number of different metal atoms and ions and small clusters of metal atoms in liquid helium, hence studying their absorption and emission spectra in the visible region. Atoms and molecules are also readily picked up by large ($N = 10^8$ atoms) He droplets, and their spectra are sensitively detected through the use of either beam depletion following absorption or laser-induced fluorescence [3].

A charged impurity is expected to strongly modify the local environment of the liquid or of the droplet: some impurities like an electron or H^- are believed to form a cavity as an effect of the repulsion which arises from the Pauli Exclusion Principle [9]. Other impurities like the alkali metal ions should form a region of increased density due to electrostriction, which means that the ensuing local density has been estimated to become so large that some kind of solid order is expected to be present. This is the so-called snowball model [11] that has been widely

[a] e-mail: fa.gianturco@caspur.it

used to interpret the experimental data. On the basis of this phenomenological model, the snowball formation is at the basis of the explanation of the very low mobility of a positive ion, which is seen experimentally, as compared with that of a neutral species such as ^{3}He. Experimentally the mobility is known to depend on the identity of the core ion. Whereas electrons form bubbles of 34 Å diameter [12,13] positive ions are surrounded by many He atoms that are strongly compressed as a result of electrostriction and smaller structures are formed. The resulting core is thought to be solid, with a diameter of about 11 Å containing about 35 He atoms: it is referred to as a snowball [14,15]. The large effective mass of the electron-containing bubbles is considered to be due entirely to hydrodynamic backflow effect [14], while the smaller mass of the snowballs is mainly that of a sort of solid core. Thus, the large diameter of the bubble formed around an electron could be explained by the strong exchange repulsion between the electron and the surrounding He atoms and can also be seen for anions [12,13]. These models have also been adapted to snowball structures to explain similar cavities formed by alkaline earth ions in liquid helium [15], but in such cases the radii of the bubbles are, however, smaller (5 to 6 Å) because of attractive electrostatic and polarization forces with the ion cores, so that the properties of such bubbles can be calculated by minimization of the total energy of the system. One of the consequences of the snowball formation is the presence of a rather low mobility in the superfluid solvent of the positive ion compared to that of a neutral dopant like ^{3}He [16]. Hence, mobility measurements can give estimates of snowball radii for species like K^+ (8.3 Å) and Cs^+ (8.4 Å) [16] with the mobility observed to decrease as the atomic number of the ion increases. There is, however, still a basic lack of microscopic models which can realistically describe the presence of local "solid" order within the liquid 'container' far from the ion [17] and which can also describe its dependence on the chemical species, especially in the case of the more complicated dopants provided by ionic molecular partners.

The aim of the present paper is therefore that of presenting detailed quantum calculations based essentially on an ab initio approach to the quantum dynamics and to the description of the quantum forces. In particular, we have chosen a polar molecular ion, LiH^+, at its equilibrium geometry of 4.142 a.u. and in its ground electronic state $X^2\Sigma^+$, and studied the adaptive formation of a snowball structure around the ionic dopant within a cluster of ^{4}He atoms.

Next section briefly outlines the employed modelling of the interaction forces while Section 3 describes the quantum dynamics we carried out to obtain structural data. Section 4 presents our results and Section 5 summarizes our conclusions.

2 The interaction potential

In the case of weakly interacting systems, e.g. when neutral dopants are embedded in He droplets, the full interaction between the dopant molecule and the solvent adatoms, together with the interactions between helium partners, is usually represented within the so-called "sum-of-potentials" approximation [18], whereby one can write

$$V(\mathbf{R},\mathbf{s}) = \sum_{i=1}^{N} V_{M-\mathrm{He}}(\mathbf{R}_i) + \sum_{i<j} V_{\mathrm{He}-\mathrm{He}}(s_{ij}) + O(V_{3B}) \tag{1}$$

where $(\mathbf{R},\mathbf{s})$ represent collectively the vectors defining the distances between the dopant M and each He atom and the vectors defining the distances between solvent atoms, respectively. To disregard the additional effects due to three-body (3B), V_{3B}, forces has therefore become one of the cornerstones for the most accepted modelling of such intermolecular forces within the droplets formed by He atoms.

In the case of ionic impurities, however, the marked increase in the strength of the intermolecular forces makes the above approximation less convincing. On the other hand, our recent study on the LiH^+–He_n systems using ab initio methods for the smaller clusters [19] has clearly shown that the many-body (MB) effects are present in such system but that their contributions to equation (1) are fairly small, at least for small n values, and therefore that the corresponding structures of the most stable bound states can be realistically described by the use of equation (1). We will thus follow the same procedure during the calculations presented here.

The terms in the first sum on the r.h.s. of equation (1) represent the highly anisotropic interaction between the ground electronic state of LiH^+ and each partner atom. The calculations [19] were carried out using the GAMESS package [20] for the ground (X^2A^1) and first excited (2^2A^1) electronic states of the $(LiHHe)^+$ system using a CASSCF molecular orbital optimization followed by an MRCI expansion. The atomic basis set for Li was that optimized in reference [21], whereas the one for H was that optimized in our earlier work and was reported in reference [19]. The atomic basis set for He was the aug-cc-pVQZ standard expansion [20] and the MRCI wave functions use single and double excitations out of a CAS reference space which includes 4 active orbitals and 5 active electrons [19].

We computed a total of 480 points given by 15 different ϑ and 32 R values for each of them. The ground electronic state, with the LiH^+ bond kept fixed at its optimum value of $4.142a_0$ (found by us with the same basis set of above for the isolated molecule and using the CASSCF plus MRCI procedure) exhibits its global energy minimum in the collinear configuration with $\vartheta = 180°$ and an R value of $4.125a_0$.

There is very little charge migration exhibited by the dopant ion bound to the He atom since we found that beyond about 6 bohr the positive charge is localized on the Li atom by ∼95% and by about 5% on the H atom, with no residual charge on the He atom. The strong orientational anisotropy is shown by the angular behavior of the interaction potential $V_{min}(R_{min},\vartheta)$ values reported by Figure 1 from reference [19]. The results shown in the

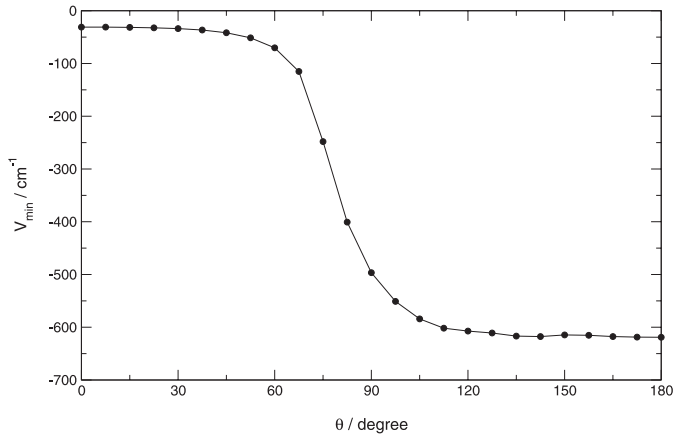

Fig. 1. Computed angular minimum energy path for the LiH^+–He intermolecular potential employed in the present work [19]: see text for details. The orientation $\vartheta = 0°$ corresponds to the H-side of the molecular ion.

figure clearly underline the marked energetic gain of the He partner when moving from the H-side to the Li^+ side of the dopant ion, as expected because of the strong induction forces existing in the system. We also see that the energy gain starts over a broad angular region, i.e. as the He atom moves beyond the T-shaped configuration towards the Li^+ nucleus the stabilization energy increases by a factor of seven over a range of less than 30°. We shall further see below how such orientational energetics affects the adaptive structuring of the solvent around the title molecule.

We have also carried out a multicenter numerical fitting of the present potential energy surface (PES), as described in detail in our earlier work [19], and finally obtained an analytic representation of the full interaction. The He–He potential energy curve was the one already employed by us before [18] and described in detail by Aziz et al. [22]: its maximum well depth is about 70 times smaller than the corresponding ionic interaction with one of the He solvent atoms.

3 The quantum Monte Carlo simulation

The implementation of the diffusion Monte Carlo approach, and its application to molecular systems such as molecular impurities in ^{4}He droplets, has been already discussed several times in the current literature [23–31], and we therefore only summarize here the main features of the method employed by us.

The time-dependent Schrödinger equation can be written in the familiar form

$$-\hbar\frac{\partial\psi(\mathbf{r},t)}{i\partial t} = (\hat{H} - E)\psi(\mathbf{r},t) \tag{2}$$

where $\mathbf{r}$ denotes collectively all the particle coordinates and E shifts the absolute energy scale of the problem at hand. As we have said above, the Hamiltonian is made up from pairwise potentials as given by equation (1) and can be written via equation (3)

$$\hat{H} = \sum_j -\frac{\hbar^2}{2m_j}\nabla_j^2 + V(\mathbf{r}). \tag{3}$$

We can now use it in expression (2) to obtain the diffusion equation for the wave function by replacing the time t with the imaginary time $\tau = -it/\hbar$

$$-\frac{\partial\psi(\mathbf{r},\tau)}{\partial\tau} = -\sum_j D_j\nabla_j^2\psi(\mathbf{r},\tau) + [V(\mathbf{r}) - E]\psi(\mathbf{r},\tau) \tag{4}$$

where $D_j = \hbar^2/2m_j$ are the diffusion coefficients. The second term on the right-hand side (rhs) of equation (4) $[V(\mathbf{r}) - E]$ is the "rate constant" or branching term. Ignoring the branching term transforms equation (4) into a simpler pure diffusion equation. It is well-known that better efficiency in the solution of equation (4) is attained if one uses importance sampling [26] that consists in constructing an analytical trial function $\psi_T(\mathbf{r},\tau)$ which approximates the true ground-state wave function and then solving the diffusion equation (4) for the mixed distribution $f(\mathbf{r},\tau) = \psi(\mathbf{r},\tau)\psi_T(\mathbf{r},\tau)$, which satisfies the equation

$$\frac{\partial f(\mathbf{r},\tau)}{\partial\tau} = \sum_j [D_j\nabla_j^2 f(\mathbf{r},\tau) - D_j\vec{\nabla}\cdot(\vec{F}\cdot f(\mathbf{r},\tau))] + [E_L(\mathbf{r}) - E]f(\mathbf{r},\tau) \tag{5}$$

where $\vec{F} = \vec{\nabla}\ln\psi_T$ is a drift force proportional to the gradient of the trial wave function. E_L is the local energy defined as

$$E_L(\mathbf{r}) = \psi_T^{-1}(\mathbf{r})\hat{H}\psi_T\mathbf{r}) = \psi_T^{-1}(\mathbf{r})\hat{T}\psi_T(\mathbf{r}) + V(\mathbf{r}). \tag{6}$$

A random walk technique is used to solve equation (5), whereby a large number of random walkers is propagated with time steps $\Delta\tau$ starting from an arbitrarily chosen initial distribution. The random displacements of the walkers when moving from τ to $\tau + \Delta\tau$ is subjected to the drift force and to a Metropolis-type acceptance algorithm [24,26,27,30]. The ground state energy E_0 is obtained by averaging $E_L(\mathbf{r})$ over the final mixed distributions $f(\mathbf{r},\tau_f) = f(\mathbf{r})$ as long as the trial function ψ_T is not vanishing in spatial regions of significant contribution to the ground-state wave function ψ_0:

$$\langle E_L\rangle = \frac{\int E_L(\mathbf{r})f(\mathbf{r},\tau_f)d\mathbf{r}}{\int f(\mathbf{r},\tau_f)d\mathbf{r}} = \frac{\int \psi_0(\mathbf{r})\hat{H}\psi_T(\mathbf{r})d\mathbf{r}}{\int \psi_0(\mathbf{r})\psi_T(\mathbf{r})d\mathbf{r}} = E_0. \tag{7}$$

Expectation values of position operators $\hat{A}(\mathbf{r})$ are also given by averaging over $f(\mathbf{r})$. The Monte Carlo walk converts the integrals over $f(\mathbf{r})$ into simple averages over the ensemble of walkers $\{w_j\}$:

$$\langle\hat{A}\rangle = \frac{\sum_j w_j\hat{A}(\mathbf{r}_j)}{\sum_j w_j}. \tag{8}$$

Direct averaging over the weighted configurations can lead, however, to mixed average $\langle\psi|\hat{A}|\psi_T\rangle$, which can contain some bias for operators $\hat{A} \neq \hat{H}$.

The potential acting within each cluster was expressed as a sum of pairwise potentials as in equation (1). The trial function used here for the He–He pairs is a product of trial wave functions

$$\Psi_t = \prod_{i,j\epsilon He} \varphi_t(r_{ij}) \tag{9}$$

where the φ_ts for the He–He pairs in each cluster were given by

$$\varphi_t(r_{ij}) = \exp\left[-\left(\frac{p_5}{r_{ij}^5} + \frac{p_2}{r_{ij}^2} + p_1 \cdot r_{ij} + p_o \cdot l_n(r_{ij})\right)\right] \tag{10}$$

and the parameters were those employed in our previous work on ionic systems [32]. The trial function for the $LiH^+ - (He)_n$ system was also given by a product of trial wave functions, each of which was given as:

$$\chi_{M-He_i}(\mathbf{r}_i) = \exp\left\{(2 + \cos\vartheta_i) \times \left[-\left(\frac{a_5}{r_{i1}^5} + \frac{a_2}{r_{i1}^2} + a_1 \cdot r_{i1} + a_0 \cdot l_n(r_{i1})\right)\right]\right\} \tag{11}$$

where $r_{i1} = \mathbf{r}_i \cos\vartheta_i$. All the parameters employed in our work are available on request from the authors.

We have propagated the diffusion equations using time steps $\Delta\tau$ of 0.5 atomic units and employed a number of steps around 7,000 a.u.$^{-1}$, reaching a number of blocks that varied, for each cluster, between 300 and 400. The binding energy found for one He atom compared well with the value obtained using our own Discrete Variable Representation (DVR) approach [33] for the same calculation: the difference was found to be about 1 cm^{-1}.

4 Discussion of results

4.1 Computed binding energies

The computed energy values obtained from the DMC calculations are reported in Table 1, where cluster sizes up to $N = 30$ are presented. All values are given in cm^{-1}. The corresponding pictorial view of the total binding energies as a function of N is further given by Figure 2.

It is interesting to note that the qualitative behavior of the binding energies is very similar to that provided by our earlier, classical calculations for n up to 7 [19] which are shown for comparison in the inset of the left-side panel. The data of Figure 2 indicate, in three different panels, several aspects of the energetics of the ionic impurity. One sees clearly an increase of the total binding energies almost linearly with N up to $N = 5$, with a marked change of the slope of the rate between $N = 6$ and 30 where a steady decrease is shown in the upper-right panel. Such changes

Table 1. Computed total binding energies E_{bind} (left column), evaporative energies E_{evap} (central column) and average binding energy per He atom (right column) from present DMC calculations. All values in cm^{-1}.

N	E_{bind} (cm^{-1})	E_{evap} (cm^{-1})	E_{bind}/N (cm^{-1})
1	–483.230 ± 1.36	483.230 ± 1.36	–483.230
2	–954.624 ± 1.78	471.394 ± 3.13	–477.312
3	–1404.005 ± 2.98	449.381 ± 4.76	–468.002
4	–1752.652 ± 3.58	348.647 ± 6.55	–438.163
5	–2089.423 ± 5.29	336.771 ± 8.86	–417.885
6	–2194.036 ± 5.83	104.613 ± 11.13	–365.600
7	–2226.288 ± 8.85	32.252 ± 14.69	–318.041
8	–2264.435 ± 8.80	38.147 ± 17.65	–283.054
9	–2294.687 ± 7.93	30.252 ± 16.73	–254.965
10	–2337.538 ± 6.94	42.851 ± 14.87	–233.754
12	–2407.077 ± 6.73	34.769 ± 13.67	–200.590
15	–2493.914 ± 1.08	28.945 ± 7.81	–166.261
17	–2538.303 ± 1.11	22.194 ± 2.18	–149.312
20	–2601.122 ± 4.71	20.940 ± 5.82	–130.056
25	–2704.247 ± 7.90	20.650 ± 13.61	–108.170
30	–2797.963 ± 7.59	18.743 ± 15.49	–93.265

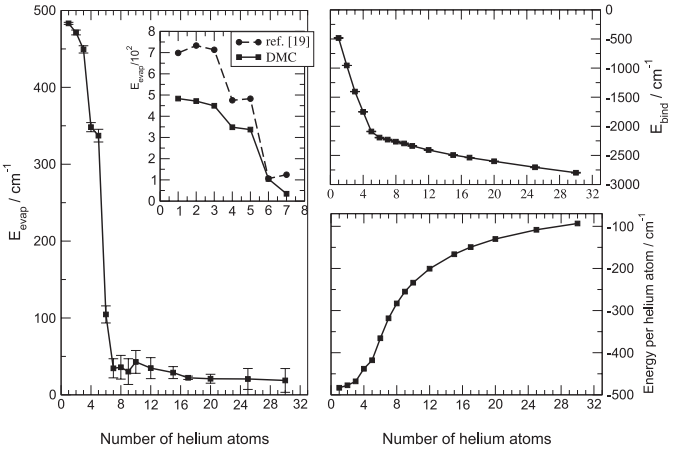

Fig. 2. Computed total binding energies (right upper panel), evaporative energies (left panel) and average binding energy per He atom (lower right panel) from present DMC calculations. All values in cm^{-1}. The inset on the left compares the present findings with the classical results of reference [19].

are likely to correspond to selective structuring of the solvent around the molecular ion, i.e. to a sort of allocation of the core of the "snowball" inside the larger droplet, as it could be also gleaned by examining the left-side panel in Figure 2. One sees there, in fact, that the evaporation energy, E_{evap}, remains nearly constant for the first three adatoms and changes by about 30% for the next two, while substantially reducing by about one order of magnitude when going to the $N = 7$ cluster. The further addition of He atoms up to $N = 30$ is seen to return a slowly changing value of E_{evap} that diminishes from around 30 cm^{-1} down to around 20 cm^{-1} for the larger clusters: the system is

clearly undergoing some sort of structural transition for n values beyond 6–7. The analysis of the corresponding radial and angular distributions will help us to clarify this point, as further discussed in the next subsection. The actual energy values, together with their error bars, are explicitly given by Table 1.

4.2 Radial and angular distributions

The radial and angular Pair Distributions (PDs) are very useful correlative observables which help us to better understand the spatial collocations of the adaptive solvent around the central dopant atom.

They are defined as:

$$P_{rad}(\mathbf{R}) = \frac{1}{N}\sum_{i=1}^{n}\left\langle \frac{\delta(|\bar{R}|_i - |\bar{R}|)}{R^2}\right\rangle_{walk} \tag{12}$$

from which one obtains the spherically averaged radial density distribution of a given atom $\rho(\bar{\mathbf{R}})$:

$$\rho(\bar{\mathbf{R}}) = \frac{N}{4\pi} P_{rad}(\bar{\mathbf{R}}). \tag{13}$$

The same procedure further attains the cosine distributions associated with any of the possible angles between the molecular center of mass and two of the He atom positions, $P_{tot}(\cos\vartheta)$, or the direct angular dependence $P_{tot}(\vartheta)$, both satisfying the normalization conditions:

$$\int_{-1}^{1} P_{tot}(\vartheta) d\cos\vartheta = 1 \tag{14}$$

or:

$$\int_{0}^{\pi} P_{tot}(\vartheta) d\vartheta = 1. \tag{15}$$

The normalized PD's for the radial and angular distributions of He atoms with respect to the molecular center-of-mass are reported by the various panels of figures that we shall discuss below, as well as the corresponding PD's functions for the He–He correlated distributions.

By looking at the radial and angular distributions of the initial He adatoms with respect to the center-of-mass located on the molecular dopant (Fig. 3) we can clearly make the following considerations:

1. up to $N = 6$, the He atoms appear to be essentially equivalent and radially located at about 2.5 Å away from the dopant (the snowball core), with the strongest binding energies to it as reported by Table 1 and in Figure 2;
2. the corresponding angular distributions favor initially the angular regions near the Li^+-end of the dopant but become rapidly more diffuse, thus starting to form an additional area with solvent atoms in the region around the T-shape configuration.

Such an highly orientational behavior can also be seen, even more pictorially, by looking at the isolines of the density distributions presented by Figure 4. We report

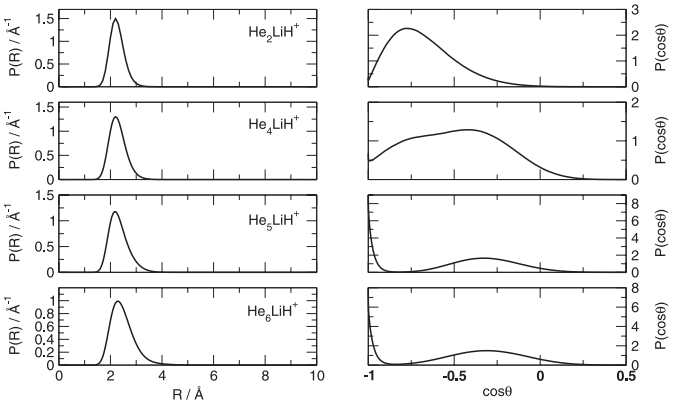

Fig. 3. Computed radial and angular PD functions for the He adatoms with respect to the molecular center of mass. Left panels: radial distributions; right panels: angular distributions. All quantities are normalized to unity.

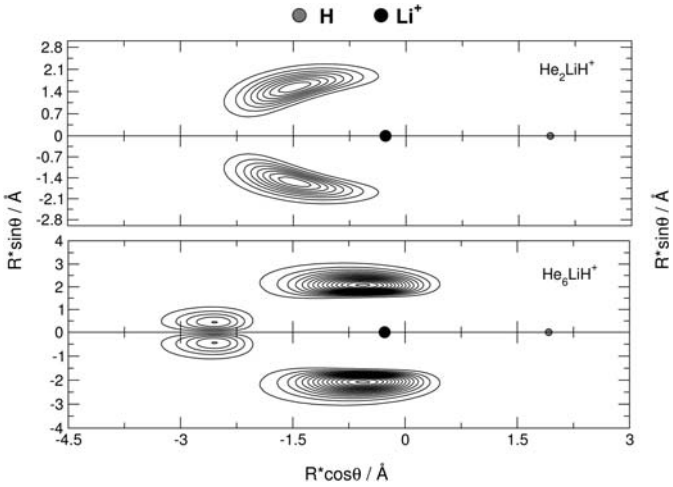

Fig. 4. Density distributions isolines plotted on the (x, y)-plane from the previous values of Figure 3. The locations of the Li^+ atom (black ball) and of the H atom (grey ball) are clearly indicated. The symmetric planes around the molecular axis are shown for clarity.

there, in fact, the density levels of such distributions in the (x, y)-plane with respect to the dopant molecular atoms, which are also indicated in each panel of that figure. The cylindrical symmetry of the real phase space is underlined by showing the ^{4}He density behavior both above and below the molecular axis. Only the $N = 2$ and $N = 6$ clusters are shown.

The density distributions of Figure 4 help us to better visualize the strongly structured nature of the ^{4}He atoms which locate themselves around the ionic dopant. For example, we can say that the initial two He atoms have largely equivalent binding energies and are placed off axis and on the ionic side of the dopant, as expected. On the other hand, as we progress to $N = 6$, we see that the additional adatoms force the distributions to split into two separate basins of collocation: one nearly collinear and the other still around the T-shaped configuration.

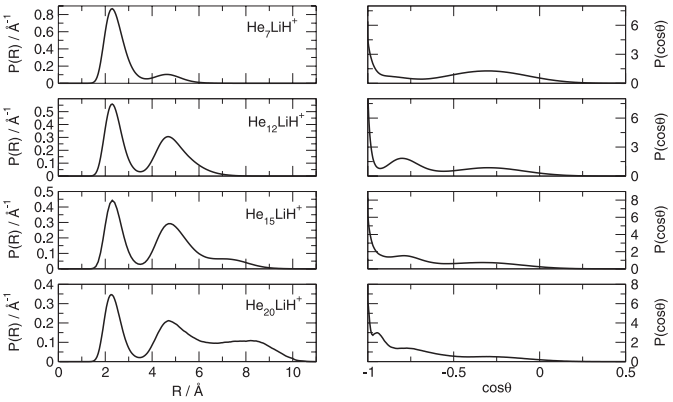

Fig. 5. Computed radial and angular PD functions as in Figure 3, but for larger values of the number of He atoms in the clusters.

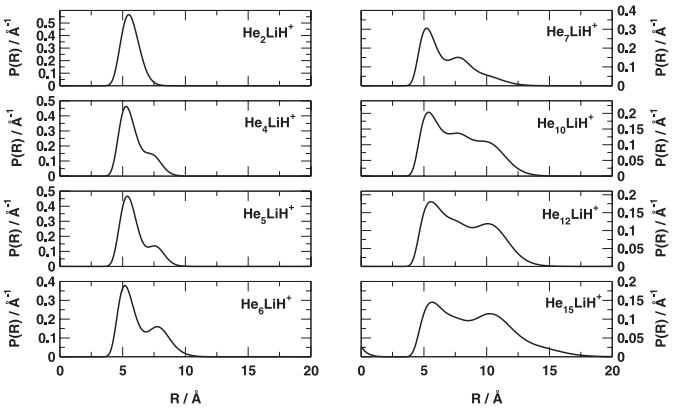

Fig. 7. Computed radial PD functions between any two He atoms in different cluster sizes. See text for further details.

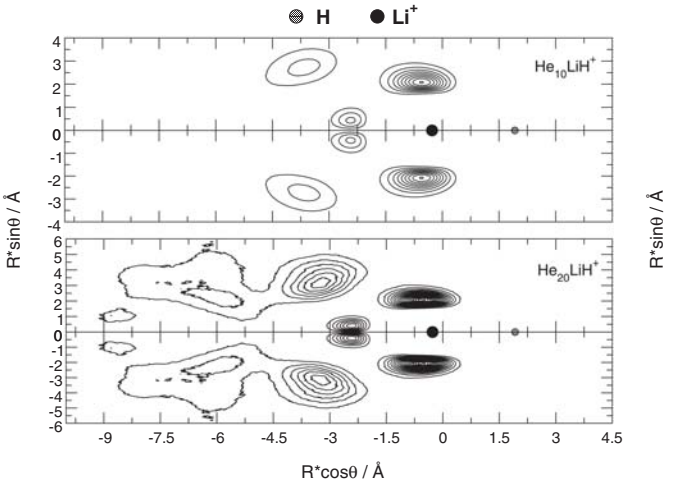

Fig. 6. Computed isolines of PD functions for the solvent atoms surrounding the dopant ion, with cluster sizes of $N = 10$ (upper panel) and $N = 20$ (lower panel).

The results shown by Figure 5 continue the analysis of the ^{4}He atom radial and angular distributions for the larger clusters, where we see that an additional, outer layer of atoms appears further away from the dopant and increases for N values up to 12. The corresponding angular distributions become even more diffuse in the sense that we now see some nonzero density distribution values to appear for the T-shaped structures, as discussed earlier.

The larger clusters beyond $N = 12$ shown in that figure further indicate the formation of as yet a third layer of adatoms which begins to show beyond about 7 Å from the dopant center-of-mass. Their corresponding angular distributions show a further density accumulation at the Li^+ center, following the growth of an highly structured region of the snowball near the linear geometry.

The data reported by Figure 6 extend the analysis of the PD isolines around the dopant ion to the larger clusters by showing such distributions for $N = 10$ and 20. The presence of a highly structured region for $N = 10$ is seen rather clearly, with the formation of three distinct basins of collocation of solvent adatoms around the ionic "head" of the dopant (top panel in the figure) which clearly shows its "heliophilic" character. As the number of solvent atoms further increases, however, we see that yet an additional area, also on the H-end of the dopant, begins to get filled by solvent atoms up to about $N = 20$, where one sees the near completion of a solvent "cap" around the ionic end of the dopant.

The analysis of the He–He PD functions, obtained by integration over all other variables, might help us to better understand the adaptive clustering in the present system: such quantities are reported by Figure 7 for some of the systems analysed in the present work. The presence of an initial area of closely packed helium atoms could be gleaned from the top two left panels in the figure, where we see such distributions up to $N = 4$. The addition of the next two He atoms leads to the formation of a second shoulder in the distributions, indicating the presence of additional atoms which locate further away from each other.

Around $N = 10$ we then see the appearance of another shell of strongly structured atoms at distances around 10 Å, while the further indication of a third basin of bound He atoms begins to be given for $N = 20$ and beyond.

Another way in which we can analyse the strongly orientational distributions offered by the solvent atoms within the snowball region is given by the data shown in Figure 8. We report there, in three different panels, the relative increase of the number of He atoms within arbitrary chosen angular regions around the dopant molecular ion. The lowest panel shows the large-angle region where the ionic head of the dopant is located: we clearly see there that it is only from $N = 5$ that the He adatoms start to occupy nearly collinear positions along the molecular axis, remaining there in constant number till the shell of $N = 12$ is completed. Then, one can clearly notice that an increase of He density is occurring along the quasi-linear collocation with respect to the LiH^+ molecule in order to close the "cap" structure mentioned before.

The intermediate range of angular values (middle panel) shows nearly unit density of adatoms till the clusters complete what appears like the first snowball shell

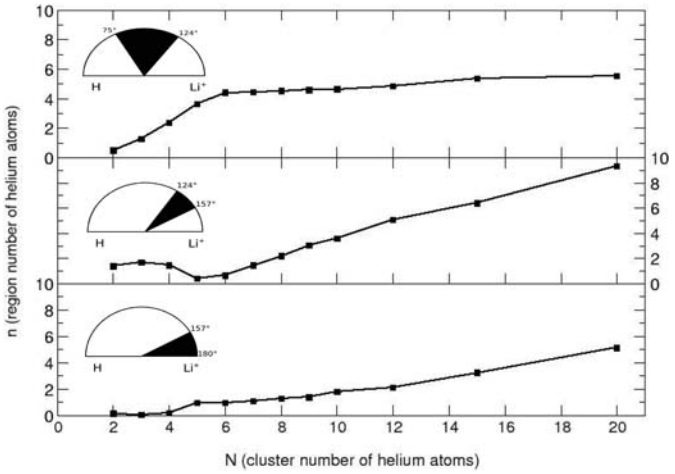

Fig. 8. Partial angular sectors of density distributions of He atoms with respect to the Jacobi angle referred to the dopant molecule. The $\vartheta = 180°$ orientation corresponds to the collinear region at the Li^+ end of the molecule. The darkened sectors in each panel show the angular ranges.

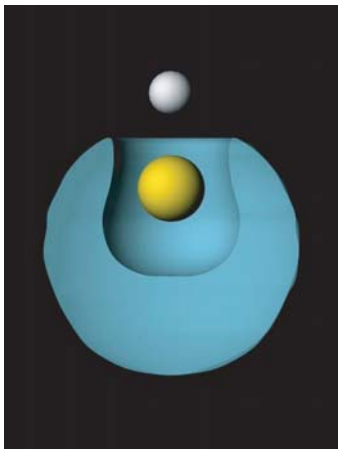

Fig. 9. (Color online) Pictorial representation of the "snowball" structure of ^{4}He atoms located around the ionic head (Li^+) of the dopant molecule.

($N = 6$). Afterwards we observe a steady growth of nonlinear collocation of He atoms with respect to the molecular axis. The top panel of Figure 8 shows helium density allocation closer to the T-shape, i.e. well off the collinear orientation. One sees there preferential positioning of the initial He atoms till the initial core is effectively completed, while for larger clusters the angular regions closer to the collinear arrangement are preferentially populated.

One interesting consideration could be had by linking the present findings to our earlier calculations of the energies and spatial distributions of all the bound states of the smallest cluster of (Li^+HHe) [7]. We had found there that the lowest bound state had clearly a collinear shape but the He adatom was symmetrically delocalized around the $C_{\infty v}$ axis, mapping an angular region similar to that of the top panel in Figure 8. Furthermore, those calculations [7] had found that the next higher bound state was a "bending" configuration with the He atom located at around 180°: this seems to suggest that a pseudosingle particle description of our smaller clusters could be profitably obtained by considering each He atom as nearly independently occupying that bent state available in the monomer. Such virtual excitation would come about because of the additional He–He repulsive interaction that removes the energetic gain of occupying only the monomer's linear ground state by more than one adatom. The corresponding many-particle wavefunction, however, will have to be constructed as a nodeless entity since it describes the ground state of the droplet atoms and is not given by the nodal structure of the single-particle states.

The highly structured nature of the initial "core" of the snowball formation could be understood by looking at the pictorial representation of the latter given in Figure 9. We show there, in fact, a cup-like area of an initial set of more strongly bound solvent atoms located around the ionic head of the dopant, followed by a less dense region of solvent atoms which represent the less perturbed droplet environment.

The classical structure optimizations of the same series of small cluster (with N up to 6) which we have also carried out earlier on [19], further confirm such a picture. We have shown in that work, in fact, that the two adatoms of the $LiH^+(He)_2$ cluster are strongly off axis with nearly C_{2v} symmetry, as indicated by our earlier Figure 4. Furthermore, we showed that, from $N = 3$ to $N = 5$, the clusters grow by placing the additional He atoms invariably off the collinear orientation and increasingly at angles close to 90° from it. Thus, the classical structures support the quantum results, albeit with the simplified language of describing well localized He atoms, a feature that the more correct quantum DMC results indicate to be missing because of the strong delocalization properties of this quantum solvent.

Beyond $N = 5$, our results of Figure 8 suggest an increasing presence of He atoms within the more collinear basin of acceptance in the clusters. The classical calculations indicate also that the $N = 6$ and $N = 7$ clusters show minimum energy structures with one and two He atoms nearly along the collinear configuration, thus confirming the present findings.

One additional way of looking at the present results is given by Figure 10, where we show the radial densities of the solvent atoms evaluated from the LiH^+ center of mass. The corresponding density in pure helium bulk is also shown. One clearly sees there the marked presence of the 'electrostriction' effects around the ionic dopant, where a marked increase of helium densities is visible from calculations. On the other hand, one also sees the presence of a nearly "normal" density beyond the initial core, with the appearance of a second maximum for the density distributions in the larger clusters. Thus, one may say that the initial "snowball" structure corresponds to a closely packed ensemble of nearly 12 ^{4}He atoms with the outer rims of such core more effectively exchanging with the

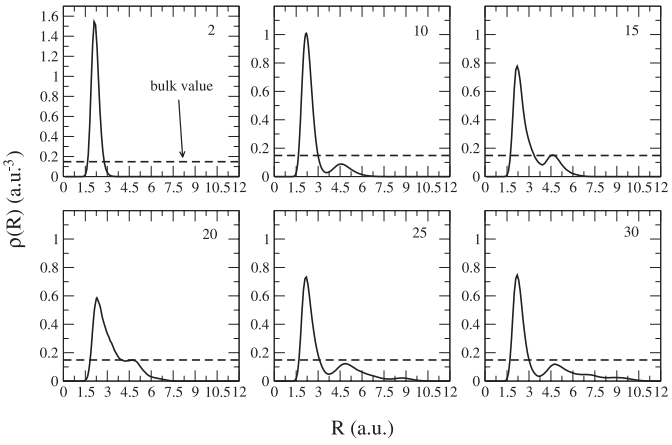

Fig. 10. Computed radial ^{4}He densities, measured from the LiH^+ center of mass, for clusters of different sizes. All values in atomic units.

bulk structure. However, because of the quantum behavior of the solvent atoms (which invariably show spatial delocalization and symmetry equivalence) we see that the next shell, before completing the one with 12 adatoms, starts already to become populated: e.g. see top second panel from left in Figure 10.

5 Present conclusions

The calculations reported in our work have tried to analyse in some detail the nanoscopic quantum structures, and their corresponding quantum energetics, of a series of ^{4}He clusters structured around an ionic dopant. The scope was to extract further information on the behavior of this quantum solvent once an ionic molecular impurity is considered to be solvated.

We employed a fully ab-initio, post-Hartree-Fock set of calculations to generate the interaction between the LiH^+ ion, taken as a rigid rotor structure, and one He atom and further constructed the full interatomic forces within clusters of arbitrary size by employing the sum-of-potentials approximation. The latter had been found in a previous study [19] to provide a realistic description of the forces at play in the cluster environment.

The quantum, ground state wavefunctions at $T = 0°$ were obtained using the DMC approach, the details of which were given in the previous section. We found the following specific features for the clusters with size of N up to 30:

1. the initial 5–6, atoms form a sort of "harder core" of solvent around the cationic part of the dopant molecule, with further 5–6 atoms also closely packed around the molecular ion;
2. the further addition of atoms up to $N = 30$ shows the formation of a sort of "cap-like" structure around the heliophilic part of the dopant ion, while the heliophobic head (the H atom) remains on the outskirts the solvated region, at least for the range of small clusters examined here. The second solvation shell appears to complete around 12 adatoms;
3. the stronger ionic interaction thus appears to drive a marked orientational behavior of the helium atoms which are seen to "crowd" themselves around the Li^+ cationic head of the dopant molecule, thereby forming there a more structured region of the cluster, as also suggested by experimental findings on ionic species [5].

This marked distinctions between the strongly solvated ionic head and the rest of the dopant molecule (albeit shown for a somewhat simple case) could perhaps be of help in selecting possible dopant species that can be used to control the cryomatrix time-of-flight by further cooling its translational motion using laser manipulation within "Coulomb crystal" configurations [34]. Thus, it could be conceivable to use the "surfactant" ionic dopant as an additional "ionic flag" which would allow velocity manipulation of the He droplets for a more detailed probing of their structures [35].

The financial support of the University of Rome Research Committee, of the MUIR research programs FIRB and PRIN and of the CASPUR supercomputing Consortium is gratefully acknowledged. The support of the European Network "Cold Molecules" (HPRN-CT-2002-00290) is also acknowledged, together with the INTAS Collaborative Project no. 03-51-6170.

References

1. E. Whittle, D.E. Dows, G.C. Pimentel, J. Chem. Phys. **22**, 1943 (1954)
2. L. Andrews, M. Moskovit, *Chemistry and Physics of Matrix Isolated Species* (North Holland, Amsterdam, 1989)
3. J.P. Toennies, A.F. Vilesov, Ann. Rev. Phys. Chem. **49**, 1 (1998)
4. J.A. Nothby, J. Chem. Phys. **115**, 10065 (2001)
5. F. Stienekemeier, A.F. Vilesov, J. Chem. Phys. **115**, 10119 (2001)
6. J.P. Toennies, A.F. Vilesov, Ang. Chem. Int. Ed. **43**, 2622 (2004)
7. E. Scifoni, E. Bodo, F.A. Gianturco, J. Chem. Phys. **122**, 224312 (2005)
8. B. Tabbert, H. Gunther, G. Zuputliz, J. Low Temp. Phys. **109**, 653 (1997)
9. V. Ghazarian, J. Eloranta, A. Apkarian, Rev. Sci. Instrum. **73**, 3606 (2002)
10. P. Claas, S.O. Mende, F. Stienkemeier, Rev. Sci. Instrum. **74**, 4071 (2003)
11. K.P. Atkins, Phys. Rev. **116**, 1339 (1959)
12. J. Jortner, N.R. Kestner, S.A. Rice, M.H. Cohen, J. Chem. Phys. **43**, 2614 (1965)
13. M. Rosenblit, J. Jortner, J. Chem. Phys. A **101**, 751 (1997)
14. M.W. Cole, R.A. Bachman, Phys. Rev. B **15**, 1388 (1977)
15. M.W. Cole, F. Toigo, Phys. Rev. B **17**, 2054 (1978)
16. W.I. Glaberson, W.W. Johnson, J. Low Temp. Phys. **20**, 313 (1997)
17. N. Takahashi, Physica B **89**, 284 (2000)
18. E. Bodo, F. Sebastianelli, F.A. Gianturco, E. Yurtsever, M. Yurtsever, J. Chem. Phys. **120**, 9160 (2004)

19. E. Bodo, F. Sebastianelli, F.A. Gianturco, I. Pino, J. Chem. Phys. A **109**, 4252 (2005)
20. M.W. Schmidt, K.K. Baldridge, J.A. Boatz, S.T. Elbert, M.S. Gordon, J.H. Jensen, S. Koseki, N. Matsunaga, K.A. Nguyen, S.J. Su, T.L. Windus, M. Dupuis, J.A. Montgomery, J. Comput. Chem. **14**, 1347 (1993)
21. A. Yiannopoulou, G. Jeung, S.J. Park, H.S. Lee, Y.S. Lee, Phys. Rev. A **59**, 1178 (1999)
22. R.A. Aziz, F.R. McCourt, C.C.K. Wond, Mol. Phys. **61**, 1487 (1987)
23. D.M. Ceperly, B. Alder, Science **231**, 555 (1986)
24. W.A. Lester, B.L. Hammond, Annu. Rev. Phys. Chem. **41**, 283 (1990)
25. R.N. Barnett, R.J. Reynolds, W.A. Lester, J. Comp. Phys. **96**, 258 (1991)
26. M. Lewerenz, R.O. Watts, Mol. Phys. **81**, 1075 (1994)
27. J.B. Anderson, Int. Rev. Phys. Chem. **14**, 85 (1995)
28. F. Paesani, F.A. Gianturco, M. Lewerenz, J.P. Toennies, J. Chem. Phys. **111**, 6897 (1999)
29. F. Paesani, F.A. Gianturco, M. Lewerenz, J.P. Toennies, J. Chem. Phys. **112**, 2239 (2000)
30. F. Paesani, F.A. Gianturco, K.B. Whaley, J. Chem. Phys. **115**, 10225 (2001)
31. F. Paesani, F.A. Gianturco, J. Chem. Phys. **116**, 10170 (2002)
32. C. Di Paola, F.A. Gianturco, Eur. Phys. J. D **35**, 513 (2005)
33. F.A. Gianturco, T. Gonzalez-Lezana, G. Delgado-Barrio, P. Villarreal, J. Chem. Phys. **122**, 084308 (2005)
34. M. Drewsen, I. Jensen, J. Lindballe, N. Nissen, R. Martinussen, A. Mortensen, P. Staanum, D. Voigt, Int. J. Mass Spectrom. **229**, 89 (2003)
35. M. Weidemueller, private communication